Simulation of the Diffusional Impedance and Application to the Characterization of Electrodes with Complex Microstructures

Hui-Chia Yu^{a,1,2}, Stuart B. Adler^b, Scott A. Barnett^c, and K. Thornton^{a,2}

Abstract

Electrochemical impedance spectroscopy (EIS) has been widely employed to probe material properties in energy materials. One important aspect of EIS is the diffusional impedance. To date, the diffusional impedance behavior is understood based on the analytical solutions of the one-dimensional (1D) diffusion equation. However, transport in materials is strongly influenced by the materials' three-dimensional (3D) microstructures that often possess complex geometries that are unlike the simplified 1D domains. In this work, we simulate the concentration response driven by oscillating loads by solving the diffusion equation in complex, experimentally determined 3D microstructures obtained from solid oxide fuel cell cathode and lithium-ion battery cathode. The simulation results demonstrate that the diffusional impedance can serve as a new technique for the evaluation of microstructural characteristics of porous media, including the tortuosity, the porosity, and the area of the loading boundary. Our findings open a new array of applications for diffusional impedance measurements.

Keywords: impedance spectroscopy, electrode microstructure, smoothed

^aDepartment of Materials Science and Engineering, University of Michigan, Ann Arbor, Michigan

^bDepartment of Chemical Engineering, University of Washington, Seattle, Washington

^cDepartment of Materials Science and Engineering, Northwestern University, Evanston, Illinois

¹Present address: Department of Computational Mathematics, Science & Engineering, Department of Chemical Engineering & Materials Science, Michigan State University, East Lansing, Michigan

²Corresponding author: kthorn@umich.edu, hcy@msu.edu

1. Introduction

Electrochemical impedance spectroscopy (EIS) is a widely used electrochemical characterization technique in many fields, including materials research and biochemistry. The measurement is carried out by perturbing the system with an oscillating voltage or current and measuring the response to the load. The resulting impedance can be decomposed into resistive, capacitive, and diffusive components, which arise from the intrinsic resistivity and charge-transfer reaction, dielectric polarization (or electric double layer), and ionic diffusion, respectively [1]. In the standard practice, the measured EIS data are fitted to equivalent circuit models to interpret the contributions from each of these contributions [2, 3]. However, in many materials, such as solid oxide fuel cell and battery electrode materials, EIS provides measurements that reflect the averaged behavior over their porous microstructures, and thus EIS fitted to a simple equivalent circuit model cannot directly determine the materials' bulk intrinsic properties. Therefore, a physics-based EIS modeling with explicit consideration of microstructures is of great importance.

While the interplay between the three contributions (resistive, capacitive, and diffusive) are important in fully understanding the electrochemical behavior of a material, probing their individual roles can offer insights and fundamental understanding between the effects of microstructures on the electrochemical behavior of materials. In this work, we present a physics-based simulation of diffusional impedance in complex microstructures. The ionic flux is dictated only by the gradient of ionic concentration and the ambipolar diffusivity due to the assumption of electroneutrality (no ionic charge separation). Additionally, the resistance for electric current is assumed to be negligibly small. These assumptions should be valid for electroneutral mixed ion-electron conductors; e.g., solid oxide fuel cell (SOFC) and some battery electrodes. For materials with considerable electron resistivity and dielectricity, a generalized expression of current must take those effects into account, as in the works of Franceschetti and Macdonald [4, 5], Barbero [6, 7], and Huang [8].

We begin with a brief introduction to the theoretical background on diffusional impedance. A measure that characterizes the diffusion flux of charge-carrier ions responding to an oscillating loading is the diffusional impedance.

In the electrochemistry community, the diffusional impedance is commonly referred to as the Warburg impedance, named after E. Warburg [9], who developed the solution for the one-dimensional (1D) diffusion equation with a sinusoidal concentration variation as the condition imposed at the boundary of a semi-infinite domain. Figure 1(a)-i illustrates the domain of diffusion for the original Warburg impedance, also called the infinite Warburg (IW) impedance. The amplitudes of the real and imaginary components of the IW impedance are equal at a given frequency. Therefore, its Nyquist plot (a plot of points set by the real and imaginary components of the impedance as the abscissa and ordinate, respectively, for a series of frequencies) forms a straight line having a 45° angle from the the abscissa, as shown by the black line in Fig. 1(b).

In many cases, the diffusion zone spans the entire sample depth of the material for which the diffusional impedance is measured. Thus, a boundary condition must be appropriately chosen for the nonloading boundary on the opposite side of the loading boundary when solving the diffusion equation. In a nonblocking-boundary case, ions can freely penetrate the nonloading boundary. The value of ionic concentration is specified at the nonloading boundary by a Dirichlet boundary condition $(C = C_B)$, as illustrated in Fig. 1(a)-ii. This boundary condition is referred to as a transmissive boundary condition (TBC). An impedance curve obtained from solving the 1D diffusion equation with TBC will exhibit a semicircle in the low-frequency region and transition to a 45° line in the high-frequency region [10, 11], shown by the blue curve in Fig. 1(b). This type of impedance is called the finitelength Warburg (FLW) impedance. A material exhibits the FLW impedance is called a Warburg short element in an equivalent electrochemical circuit that models the electrochemical system being examined. The DC response of a FLW element is characteristic of a resistor, and thus a FLW element is described as resistive. In contrast, in a blocking-boundary case, ions cannot penetrate the nonloading boundary. Thus, a no-flux Neumann boundary condition $(\partial C/\partial x = 0)$ is imposed at the opposite nonloading boundary, which is referred to as the reflective boundary condition (RBC). See Fig. 1(a)-iii for illustration. (The term "reflective" arises from the fact that such a boundary condition is typically implemented by reflecting the concentration value across the boundary into the "ghost zone," a point just out side of the physical domain.) The impedance curve in this case will consist of a vertical straight line in the low-frequency region and again a 45° line in the high-frequency region [12], shown by the red curve in Fig. 1(b). This type of impedance is called the finite-space Warburg (FSW) impedance [13, 14, 15]; materials/material elements exhibiting FSW behavior are called Warburg open elements in an equivalent electrochemical circuit. The impedance response of a FSW element is characteristic of a capacitor, and thus a FSW element is described as capacitive. The boundary condition at the nonloading boundary in a 1D case can be expressed generally as

$$D\frac{\partial C}{\partial x}\Big|_{x=L} = -k(C(L) - C_B), \tag{1}$$

where k is a permeability coefficient, x = L is the position of the nonloading boundary, C is the concentration, D is the diffusivity, and C_B is the charge carrier concentration outside the boundary. TBC is equivalent to setting $k = \infty$, which leads to $C(L) = C_B$. On the other hand, RBC is equivalent to setting k = 0. Here, we set $C_B = 0$ for the clarity of derivation. Note that k will be the reaction rate constant if in the context of charge-transfer reaction occurring at electrolyte-electrode interface.

The FLW and FSW impedances are used as the standards for fitting experimentally measured curves to evaluate the ionic diffusivities in materials, where diffusion is assumed to occur one-dimensionally. However, ionic transport in electrochemical materials usually occurs in three dimensions at the microstructural level. For example, SOFC electrodes are highly porous, and thus oxygen vacancies must diffuse through a three-dimensional (3D) complex microstructure that consists of connected ceramic particles. Li-ion battery electrodes are also comprised of irregular-sized/irregular-shaped ceramic particles that release and accommodate Li ions during the charge-discharge process. The microstructures strongly influence the transport processes in these materials. Thus, consideration of diffusion beyond 1D in microstructures is important in developing a full understanding of the diffusional impedance of energy materials.

The effects of geometries on impedance have been noted for decades, and researcher have attempted to account for these effects in impedance modeling. However, these efforts are primarily limited to equivalent circuit modeling [16, 17, 18, 19, 20, 21, 22, 23, 24]. In physics-based modeling, the microstructure effects can only be taken into account via the use of macro-homogeneous properties, such as tortuosity and porosity, in conventional porous-electrode-theory-type electrochemical simulations [25, 26, 27]. To explicitly consider diffusion through the electrode particles, the structure must be very simple due to the computational cost [8]. Song and Bazant

[28] calculated the diffusional impedance of planar, cylindrical, and spherical battery electrode particles using semi-analytical methods and compared the results to highlight the impact of geometric effect. They also demonstrated the importance of anisotropic transport in the diffusional impedance [29]. For more complicated particle geometries, Kreller et al. [30] treated SOFC cathodes as series of connected spheres and simulated the concentration response in the spheres under oscillating loadings. The work indicated that the microstructures affect the impedance behavior. However, these simulations were still based on relatively simple geometries. Cho et al. [31] considered more complex geometries of artificially generated electrode microstructures. They were able to predict the impedance behavior based on the effective material properties that were calculated based on the microstructures, but they did not provide the direct link between the microstructure and impedance spectrum. Recently, Cooper et al. [32] used a voxel-based method [33] to calculate the diffusional impedance of complicated geometries of porous electrodes. Interestingly, their work demonstrated that porous media with identical macro-homogeneous structural properties (i.e., tortuosity and porosity) can still lead to significantly different diffusional impedance. However, as pointed out in Ref. [34], the roughness of the interfaces in the voxel-based method could introduce significant numerical errors in the calculations. Therefore, further examination of the linkage between complex microstructures and impedance spectra is needed.

In this work, we demonstrate a new approach based on the smoothed boundary method (SBM) [34] to explicitly solve the diffusion equation within an experimentally obtained complex 3D SOFC cathode microstructure and use the simulation results to construct the diffusional impedance curves of the microstructure for both the TBC and RBC cases. The SBM is employed to circumvent the difficulties in solving the governing differential equations within complex geometries encountered in the conventional methods. Our results demonstrate that the diffusional impedance can be used to probe microstructural characteristics. Specifically, the diffusional impedance of microstructures with TBC can be used to determine the tortuosity of the diffusion zone in the materials being examined. This condition can arise in electron-blocking impedance measurements of battery electrodes [35], in which charge-transfer reactions are prevented, or in diffusion-dominant cases where the dynamics is governed by ionic diffusion. Furthermore, we demonstrate that the impedance with RBC can be used to quantify the porosity of the microstructure as well as the area of the loading boundary. In cases

where diffusion time is shorter than that of reaction (e.g., high-frequency regimes), the presented technique can be applied to probe the area of active particle surfaces. Finally, the diffusional impedance is calculated with RBC using a battery cathode microstructure to demonstrate the approach. The simulation results resemble experimentally measured impedance spectrum of battery electrodes such as those found in Ref. [36, 23].

The insights gained from this work opens doors for new applications of diffusional impedance measurements beyond the traditional measurements of the ionic diffusivities. Although we exclude other effects than the bulk diffusion, this work represents a step forward in quantitative modeling of impedance response with explicit consideration of complex microstructures of such electrodes.

2. Model and Formulation

As in the formulation of calculating Warburg impedance, we assume that diffusion in solids is described by Fick's second law:

$$\frac{\partial C}{\partial t} = \nabla \cdot D\nabla C \quad \in \Omega, \tag{2}$$

where t is time and Ω denotes the domain of solid. This equation can also be obtained from the Nernst-Planck equations with the assumption of electroneutrality. The Nernst-Planck equations are given by [8, 37]

$$\frac{\partial C_{+}}{\partial t} = -\nabla \cdot \mathbf{j}_{+} = \nabla \cdot \left(D_{+}^{chem} \nabla C_{+} + \frac{z_{+} u_{+}}{RT} C_{+} \nabla \Phi \right), \tag{3a}$$

$$\frac{\partial C_{-}}{\partial t} = -\nabla \cdot \mathbf{j}_{-} = \nabla \cdot \left(D_{-}^{chem} \nabla C_{-} + \frac{z_{-}u_{-}}{RT} C_{-} \nabla \Phi \right), \tag{3b}$$

where the subscripts ' \pm ' denote quantities associated with positive and negative charge carriers, $\mathbf{j}_{\pm} = -u_{\pm}C_{\pm}\nabla\mu_{\pm}$ is the ionic flux (μ_{\pm} is the electrochemical potential of ions), D_{\pm}^{chem} is the chemical diffusivity that includes a thermodynamic factor, z_{\pm} is the charge number, u_{\pm} is the mobility, R is the ideal gas constant, T is the absolute temperature, and Φ is the electrostatic potential. In an electroneutral material, $C_{+} = C_{-} = C$. Following the derivation in Refs. [8, 37], Eq. (3a) reduces to Eq. (2) with $D = (z_{+}D_{+}D_{-}^{chem} - z_{-}D_{-}D_{+}^{chem})/(z_{+}D_{+} - z_{-}D_{-})$, where $D_{\pm} = u_{\pm}/RT$ is the diffusivity at the dilute limit. In materials where negative charge carriers

diffuse much faster than cations $(D_{-} \gg D_{+})$, the ambipolar diffusivity, D, is approximately the cation chemical diffusivity: $D \approx D_{+}^{chem}$.

To predict the concentration evolution in a complex microstructure based on Eq. (2), we employ the smoothed boundary method [34], wherein a continuous domain parameter is utilized to define the solid regions. The domain parameter, ψ , is set to be one within the solid regions, and zero in the pore regions. The value of ψ transitions from one to zero across the solid surface. This transition region smears the infinitely thin surface to a diffuse interface with a finite thickness, which implicitly defines the location of the boundary; thus it is named the smoothed boundary method. To maintain numerical accuracy, the interfacial thicknesses must be thin relative to the feature sizes of the bulk [34]. Multiplying Eq. (2) with ψ and applying the product rule of differentiation, we obtain

$$\psi \frac{\partial C}{\partial t} = \nabla \cdot \psi D \nabla C - \nabla \psi \cdot D \nabla C = \nabla \cdot \psi D \nabla C + |\nabla \psi| \vec{n} \cdot \vec{j}, \tag{4}$$

where $\vec{n} = \nabla \psi / |\nabla \psi|$ is the inward unit normal vector of the surface and $\vec{j} = -D\nabla C$ is the diffusion flux. The last term is only nonzero if there is a surface flux, such as when there is a surface reaction. Since here we focus on investigating the effect of tortuous diffusion pathways in the solid regions on the diffusional impedance of a porous cathode microstructure, we set the last term in Eq. (4) to be zero as in Ref. [32]. Thus, we obtain our governing equation as

$$\psi \frac{\partial C}{\partial t} = \nabla \cdot \psi D \nabla C. \tag{5}$$

When Eq. (5) is solved, Eq. (2) is recovered within the solid phase where $\psi=1$ with a no-flux boundary condition automatically imposed on the solid surface where $0<\psi<1$ [34]. Note that ψ is used to set the boundary condition at the solid-pore interface only; the boundary conditions at the computational domain boundaries are set in a conventional manner (i.e., using ghost zones).

As in Ref. [9], we solve the concentration response within the solid region under the boundary condition of an oscillating loading on the x=0 face of the computational domain. Expressing the time-dependent part by complex exponential functions, the concentration is written as $C = (\tilde{C}e^{i\omega t} + \tilde{C}^*e^{-i\omega t})/2$ [38], where $\tilde{C} = C_R + iC_I$ is a function of position (the functions C_R and C_I are the real and imaginary components of \tilde{C} , respectively), i is the imaginary unit, \tilde{C}^* is the complex conjugate of \tilde{C} , and ω is the angular frequency.

Substituting this expression of concentration into Eq. (5) and collecting terms of the real and imaginary components, we obtain two coupled equations: $\nabla \cdot \psi D \nabla C_R = -\psi \omega C_I$ and $\nabla \cdot \psi D \nabla C_I = \psi \omega C_R$, where the complex exponential functions have been canceled. These equations are nondimensionalized with a characteristic length, l, and the diffusivity, D, such that

$$\hat{\nabla} \cdot \psi \hat{D} \hat{\nabla} C_R = -\psi \hat{\omega} C_I, \tag{6a}$$

$$\hat{\nabla} \cdot \psi \hat{D} \hat{\nabla} C_I = \psi \hat{\omega} C_R, \tag{6b}$$

where the hat (\wedge) denotes dimensionless quantities, $\hat{D} = D/D = 1$, and $\hat{\nabla} = l\nabla$, and $\hat{\omega} = \omega l^2/D$. In the bulk where $\psi = 1$, these equations reduce to the governing equations in Refs. [32, 8], but they differ in that the boundary conditions are set automatically at the smooth interfaces.

Equation (6) is solved using the finite difference method on a standard Cartesian grid. The second-order differential operator is discretized using the scheme in Ref. [34]. The alternating-direction line-relaxation (ADLR) method [34, 39, 40] is employed to solve each of Eqs. (6a) and (6b), which utilizes a tridiagonal matrix solver to obtain the values of concentration along individual columns in the x, y, and z directions. While Eqs. (6a) and (6b) are solved separately, an iterative scheme is employed to find the solution that satisfies both of the equations. At a given frequency value, within each iterative step, C_R is first solved according to C_I on the right-hand side of Eq. (6a). Next, the values of C_I is solved according to Eq. (6b), with C_R obtained earlier. This procedure is repeated until both C_R and C_I are numerically converged.

In the cases of calculating capacitive diffusional impedance of battery electrodes, the oscillating ionic concentration is specified on the electrode particle surface [28], for which the SBM equations [34] become

$$\psi \hat{\nabla} \cdot (\psi \hat{D} \hat{\nabla} C_R) - D \left[\nabla \psi \cdot \nabla (\psi C_R) - |\nabla \psi|^2 C_R^B \right] = -\psi \hat{\omega} C_I, \quad (7a)$$

$$\psi \hat{\nabla} \cdot (\psi \hat{D} \hat{\nabla} C_I) - D \left[\nabla \psi \cdot \nabla (\psi C_I) - |\nabla \psi|^2 C_I^B \right] = \psi \hat{\omega} C_R, \tag{7b}$$

where C_R^B and C_I^B are the boundary values for Dirichlet boundary conditions imposed on the particle surfaces. These equations can be solved using the same iterative scheme mentioned above. Note that while the numerical method presented here is applicable to simulations with nonconstant diffusivities, we set a constant D in our simulations for the clarity of extracting the relationship between microstructures and the resulting impedance.

3. Results

3.1. Porous SOFC cathode microstructure

We use an experimentally reconstructed porous SOFC cathode as the input geometry for the simulations. This microstructure is acquired via the focus-ion-beam scanning-electron-microscopy (FIB SEM) technique. The sample, containing gadolinium-doped ceria (GDC) electrolyte and lanthanum strontium cobaltite (LSC) cathode, was milled using FIB layer by layer. SEM images were taken for individual layers. The complex porous microstructure was reconstructed by stacking all images in the depth direction, as schematically illustrated in Fig. 2(a). The reconstructed microstructure is represented by a 3D array consisting of $261 \times 321 \times 297$ voxels with the resolution of 25 nm per voxel edge. The experimental details of obtaining this porous microstructure can be found in Ref. [41]. Here, because we only focus on the diffusion in the cathode microstructure in this work, the region between the two vertical cyan planes in Fig. 2(a), which contains no electrolyte phase, is selected for our simulation. Figure 2(b) shows the cropped microstructure represented by a $176 \times 321 \times 297$ voxel array, spanning 4.40 μ m, 8.03 μ m, and 7.43 μ m in the x, y, and z directions, respectively, in which voxels having values of one indicate LSC phase, while those with zero indicate the pore phase.

To ensure accuracy in the simulations, we double the grid resolution from the voxel array. The centers of original voxels are utilized as the original grid points, and between each adjacent grid points a new point is inserted. The value at the new point is linearly interpolated from its neighboring original points. Thus, the computational domain contains $352 \times 642 \times 594$ grid points, with the grid spacing of 12.5 nm. For the SBM, a continuous domain parameter is required. The voxel values are first smoothed using Allen-Cahn dynamics with 20 steps at the maximum stable time step size, followed by the level-set distancing scheme, similarly to the process described in Ref. [42]. Taking the hyperbolic tangent of the resulting values [34], the domain parameter, ψ , is obtained. Figure 2(c) shows the microstructure depicted by the isosurfaces of $\psi = 0.5$. The value of ψ is uniformly one in the LSC phase and uniformly zero in the pore phase. The surface of LSC is described by $0 < \psi < 1$, which occupies approximately 3 grid spacings across.

The volume of the LSC phase is 167 μ m³, calculated by summing the values of ψ multiplied by the voxel volume, and the area of LSC surfaces is 727 μ m², calculated by summing all triangular patches generated by Matlab[®]

of the isosurfaces at $\psi = 0.5$. Thus, the volume fraction and surface area per volume are approximately 0.63 and 4.35 μm^{-1} , respectively, in this sample. The surfaces on the six faces of the computational domain in Fig. 2(c)) are added for visualization only and thus do not contribute to the calculated surface area.

In the manner similar to Ref. [38], we choose the characteristic length scale to be $l = 0.46 \mu \text{m}$ for Eq. (6), which is the radius of a cylinder with the same surface area per volume. This equivalent radius of the microstructure spans approximately 37 grid spacings, which is larger than ten times the thickness of the diffuse interface, ensuring a sufficient accuracy for SBM [34].

3.2. Model Validation

In this section, we first validate the 3D SBM solver using a pseudo-1D simulations (i.e., effectively 1D, but calculated in a 3D domain) against the analytical solution of the Finite-Length Warburg (FLW) impedance. We then calculate the diffusional impedance for three simple 3D geometries to demonstrate the geometric impact on the resultant impedance.

3.2.1. Pseudo-1D Simulation

In the pseudo-1D case, the value of ψ is set to be uniformly one within the entire computational domain. For the boundary conditions, C_R is set to be one and zero at x = 0 and 9.67, respectively, while C_I is zero on both of the two faces [38]. Note that the coordinate variables have been normalized to l and are dimensionless. No-gradient boundary conditions are imposed on the remaining four faces of the computational domain.

Figures 3(a)-i and ii show the simulated distributions of C_R and C_I , respectively, at the scaled dimensionless frequency of $\hat{\omega}_L = 2.65$ (close to $\hat{\omega}_m = 2.54$, the dimensionless frequency at which the imaginary part of the impedance is maximum for FLW diffusion), where $\hat{\omega}_L = \omega L^2/D = \hat{\omega}L^2/l^2$ and L = 9.67l is the domain size along the primary diffusion direction. The value of C_R monotonically decreases from one to zero along the x-direction across the domain, while C_I has a minimum at the location near x = 4. The concentration amplitude profiles along the x axis are provided in Fig. 3(c), obtained by averaging C_R and C_I in each y-z plane. Although a slight bend in the C_R profile is observed due to the coupling between C_R and C_I , it is still almost linear at this frequency near the maximum imaginary component of impedance.

As the loading frequency increases, the gradients of C_R and C_I near the loading boundary (x = 0) become steeper and both C_R and C_I exhibit a minimum on their profiles, as shown in Figs. 3(b) and (d), not just C_I . The position of the minimum for C_I is much closer to the loading boundary compared to that of C_R . By solving Eq. (2) in 1D with a sinusoidal load at x = 0, the FLW impedance can be analytically derived. With the transmissive boundary condition (C = 0 at x = L) corresponding to the FLW element, the dimensionless impedance is [10, 11, 43, 44]

$$\frac{Z^{\text{FLW}}}{Z_0} = \frac{1}{L} \sqrt{\frac{D}{i\omega}} \tanh\left(\sqrt{\frac{i\omega}{D}}L\right) = \frac{\tanh\sqrt{i\hat{\omega}_L}}{\sqrt{i\hat{\omega}_L}},\tag{8}$$

where $Z_0 = RTL/z^2F^2DAc_0$ is the resistivity of the material, z is the charge number, F is the Faraday constant, A is the nominal cross-sectional area perpendicular to the principal diffusion direction, and c_0 is the equilibrium concentration of charge carriers. As mentioned earlier, D that also appears in Z_0 is set to be constant. The function of Z^{FLW}/Z_0 is plotted as the black curve in Fig. 3(e).

For the pseudo-1D simulation, the impedance is calculated according to

$$Z = \frac{RT}{z^2 F^2 D c_0} \frac{\tilde{C}|_{x=0} - \tilde{C}|_{x=L}}{\int \tilde{J}_x dA|_{x=0}} = Z_0 \frac{(\tilde{C}|_{x=0} - \tilde{C}|_{x=L})/L}{\int \tilde{J}_x dA|_{x=0}/A},$$
 (9)

where $\tilde{J}_x|_{x=0}=-\hat{D}\partial\tilde{C}/\partial x|_{x=0}$ is the flux in the x-direction across the loading boundary. Here, because $\hat{D}=1,\;\int \tilde{J}_x dA|_{x=0}/A$ is the negative of concentration gradient along the x-direction at x=0 averaged over the loading boundary. Note that we set $\tilde{C}|_{x=0}=1$ and $\tilde{C}|_{x=L}=0$ as the boundary conditions, as mentioned earlier. The calculated dimensionless impedances, Z/Z_0 , at various frequencies (from $\hat{\omega}_L=0$ to 89.07) are marked with red circles in Fig. 3(e). It is evident that calculated impedance using the pseudo-1D setup closely matches the analytical FLW impedance. Here, we do not simulate the very high frequency regime because it requires finer grid spacings to resolve very sharp gradients.

At low frequencies, the impedance curve follows a semicircle (see the region of $1/3 < \text{Re}(Z)/Z_0 < 1$). This curve transitions to a line as the frequency continuously increases, and eventually becomes a straight 45°-angle line corresponding to the infinite Warburg impedance (see the region of $\text{Re}(Z)/Z_0 < 0.2$ corresponding to $\tilde{\omega}_L > 20$). The presence of nonzero C_I

indicates that the oscillation of concentration away from the loading boundary begins to shift in phase due to the delay in the response. The transition from a semicircle to straight line occurs when the concentration amplitudes decay to zero over the domain (and thus the gradient of the concentration is negligible). As the frequency further increases, the phase shift becomes significant, and C_R and C_I have both positive and negative values in their profiles. For example, as in Fig. 3(d), C_I has negative values in the region where 0 < x < 4.52 and has positive values in the region where 4.52 < x < 9.67.

3.2.2. Simple Geometry Simulations

Figures 4(a) through (c) show a cylinder, cone, and sphere, respectively, for each of which diffusional impedance was calculated, along with the imaginary component of the concentration amplitude C_I , which will be discussed later. (A quarter of the object is made transparent to show the internal profile of C_I). These geometries are chosen similar to those in Ref. [32]. Here only qualitative comparisons of the calculated impedance spectra are made since the exact geometric dimensions in Ref. [32] are not available for a direct comparison. The domain parameter, ψ , is set to one within the geometries and zero outside. The sizes of cylinder and cone are set so that they have the same volume; specifically, the radius of the cylinder is 1.22 and the base radius of the cone is 2.12, respectively, and both have an axial length of 7.06. The sphere diameter is chosen to 7.06 such that its maximum distance from the loading boundary is equal to those in the other two cases. The $y \times z$ dimensions of the computational domains for the cylinder, cone, and sphere are 2.83×2.83 , 4.90×4.90 , and 7.62×7.62 , as shown in Fig. 4(a), (b), and (c), respectively. Both RBC and TBC calculations are performed. In the RBC calculations, the domain size in the x-direction is 7.62, and the cylinder has a closed end cap at x = 7.06. Thus, none of the three geometries contacts the nonloading boundary, and the SBM automatically imposes the RBC in the calculations. On the other hand, in the TBC calculations, the domain sizes are truncated to 6.98 in the x-direction to ensure the geometries contact the nonloading boundaries. Also note that, different from the pseudo-1D calculation, we here have $J_x = -\psi D\partial C/\partial x$ in the denominator of Eq. (9), where ψ accounts for the fact that diffusion occurs only within the solid region where ψ is nonzero.

The TBC impedance curves for these three geometries are presented in Fig. 4(d). As expected, the TBC impedance of the cylinder (marked with green circles in the magnified view in Fig. 4(e)) behaves identically to the

pseudo-1D case. When the impedance is calculated using only the the cylinder cross-sectional area (by setting $A = \pi r^2$ in Eq. (9) instead of the nominal cross-section area of the computational domain, where r = 1.22), the calculated curve (marked with gray circles) overlap the analytical FLW curve (the black curve), which again verifies the accuracy of the presented solver. The TBC impedance of the cone geometry (the blue circles in Fig. 4(d)) at low frequencies is much larger than that of the cylinder because the small contact area at the nonloading boundary hinders the fluxes from passing the nonloading boundary. In the intermediate frequency range, the gradually decreasing cross-sectional area along the x-direction limits the flux in the primary diffusion direction over the penetration depths [32] $(L_D = \sqrt{\hat{D}/\hat{\omega}_L})$, the diffusion distance corresponding to the time period of a given oscillation frequency). As a result, the calculated impedance values are still much larger than those at the same frequencies in the cylinder case, resulting in a curve showing a nearly semicircular shape, which is significantly different from those of the cylinder case. In contrast, at high frequencies, the difference between the TBC impedance curves of the cylinder and cone geometries becomes less pronounced (see Fig. 4(e)), both exhibiting infinite Warburg impedance behavior. The TBC impedance of the sphere (marked with purple circles in Fig. 4(e)) exhibits two humps, similar to that in Ref. [32]. At low frequencies, the long penetration depth reach the region near the nonloading boundary, where the circular contact area is small. Thus, the impedance in this regime is large, as in the cone case. At high frequencies, the short penetration depth probes the region near the loading boundary. Unlike the cone case, the spherical geometry has a small contact area at the loading boundary as well, which leads to a large impedance. On the other hand, the penetration depth at intermediate frequencies probes the region where the circular cross-section of the sphere is significantly larger than the contact areas at the loading or nonloading boundaries, thus resulting in a smaller impedance indicated by the valley on the Nyquist plot in Fig. 4(e). These trends result in the observed two humps in the impedance curve for the spherical-geometry case.

The calculated RBC impedance curves of the cylinder, cone, and sphere are shown in Fig. 4(f) and (g), the latter of which is a magnified view of the former. The dimensionless analytical FSW impedance [12]

$$\frac{Z^{\text{FSW}}}{Z_0} = \frac{1}{L} \sqrt{\frac{D}{i\omega}} \coth\left(\sqrt{\frac{i\omega}{D}}L\right) = \frac{\coth\sqrt{i\hat{\omega}_L}}{\sqrt{i\hat{\omega}_L}}.$$
 (10)

is also plotted with the black curve on the same figure. At low frequencies, the analytical curve of Z^{FSW}/Z_0 approaches a vertical straight line at $Re(Z)/Z_0 = 1/3$. At high frequencies, the curve becomes a straight line along 45° in the region where $\text{Re}(Z)/Z_0 < 0.2$, as in the case of FLW because the boundary condition on the nonloading boundary becomes unimportant at high frequencies due to the short penetration depth. The RBC impedance curve of the cylinder (marked with green circles in Fig. 4(f)) has a similar shape to the analytical FSW curve. When calculated using the cylinder cross-sectional area, the obtained impedance values (marked with gray circles) coincide the analytical values, which again verifies the accuracy of the 3D SBM solver. In Fig. 4(g), the RBC impedance curve of the cone (marked with blue circles) is located on the upper left side to the cylinder case and with a blunt, smooth transition from low to high frequency regions. The RBC impedance of the sphere (purple circles) is larger than that of the cylinder: the impedance curve resides on the right to that of the cylinder. The impedance at low frequencies forms a vertical line as in the other two RBC cases, but it transitions through a semicircle-like curve to the high frequency regime. This semicircle is attributed to the same mechanism causing the second hump in the TBC case (purple circles in Fig. 4(e)). The simulated C_I at $\hat{\omega}_L = 256$ (the last point in the RBC calculations) in the cylinder, cone, and sphere are provided in Fig. 4(a) through (c), respectively. The C_I distributions in the three figures are overall similar to that in Fig. 3(b)-ii, showing a rapid decrease near the loading boundaries and arising back away from the loading boundaries. In summary, the simulation results of simple geometries here generally agree with those in Ref. [32], thus validating the presented model and numerical solvers.

3.3. Porous Cathode with Nonblocking Boundary

In order to simulate diffusion in porous cathode, we substitute the ψ function obtained in Section 3.1 into Eq. (6), and solve for the concentration distribution within the complex microstructure at various frequencies. The boundary conditions on the computational domain boundaries are the same as in Section 3.2, and the impedance is calculated using Eq. (9) with $\tilde{J}_x = -\psi \hat{D} \partial \tilde{C}/\partial x$. Figure 5(a) shows the impedance curve of the calculated Z/Z_0 for $0 < \hat{\omega}_L < 109.45$ (green circles), along with $Z^{\rm FLW}/Z_0$ given by the analytical expression in Eq. (8) (the black curve). The impedance curve significantly deviates from the FLW result, as indicated by the gray arrows. We

will utilize the generalized form of effective diffusivity of the porous solid, defined below, to examine the underlying mechanism for this deviation.

The ultimate goal of this section is to relate the simulation results to microstructural characteristics such as porosity and tortuosity. These quantities have previously been linked to effective diffusivity, rather than impedance. Following the phenomenological approach used to define an effective diffusivity at the steady state [45], we define a generalized complex effective diffusivity as in

$$-\tilde{D}_{eff}\frac{\tilde{C}|_{x=L} - \tilde{C}|_{x=0}}{L} = \tilde{J}|_{x=0},$$
(11)

where the tilde (\sim) on \tilde{D}_{eff} indicates a complex quantity. The steady state here is the state that the amplitudes of concentration and flux are constant. On the left-hand side, $(\tilde{C}|_{x=L}-\tilde{C}|_{x=0})/L$ is the overall concentration gradient across the sample thickness L. The right-hand side of Eq. (11) is the macroscopic flux at x=0, which, as in Eq. (9), is the average concentration gradient along the x-direction on the loading boundary. Here, $\tilde{J}|_{x=0}=\int \tilde{J}_x dA|_{x=0}/A$, where $\tilde{J}_x=-\psi\hat{D}\partial\tilde{C}/\partial x$ and A is the nominal cross-section area. By comparing Eq. (11) with Eq. (9), we obtain the relationship:

$$\frac{Z}{Z_0} = \frac{1}{\tilde{D}_{eff}},\tag{12}$$

where the reciprocal of the complex effective diffusivity is the impedance. Here, unlike the traditionally defined diffusivity, \tilde{D}_{eff} varies with frequency.

Figure 5(b) shows the Bode plot of the amplitude (green circles), real (blue dashed line) and imaginary (red dashed line) parts of the calculated impedance. Note that the horizontal axis is in logarithmic scale and thus the first data point (the left most) shown in the figure is the smallest nonzero frequency examined ($\hat{\omega}_L = 0.034$), as zero frequency corresponds to its logarithm being negative infinity. At $\hat{\omega}_L = 0$ (direct current (DC) loading), $\tilde{D}_{eff} = 1/2.35 = 0.42$, which lead to $\tau = 1.22$ for the tortuosity of this microstructure, calculated using $\tau^2 = \hat{D}\varepsilon_v/\tilde{D}_{eff}$ [46]. While we have assumed the dimensionless intrinsic bulk diffusivity, \hat{D} , to be 1, the choice of the value does not affect the result because it cancels out. The volume fraction of the solid phase for the structure was calculated to be $\varepsilon_v = 0.63$. Note that the diffusivities at DC loading have only real components.

We now extend the expression for tortuosity to an effective tortuosity under AC loading, in which the imaginary component of effective diffusivity is nonzero, as

$$\tau_{eff}^2 = \frac{\left| \tilde{D}^{\text{FLW}} \right| \varepsilon_v}{\left| \tilde{D}_{eff} \right|}.$$
 (13)

Here, \tilde{D}^{FLW} is the complex diffusivity for 1D bulk diffusion from the analytical expression obtained from Eq. (8):

$$\tilde{D}^{\text{FLW}} = \frac{Z_0}{Z^{\text{FLW}}} = \sqrt{i\hat{\omega}_L} \coth \sqrt{i\hat{\omega}_L}.$$
 (14)

The effective tortuosity as a function of frequency is plotted with the black curve in Fig. 5(c). The value of τ_{eff} transitions from 1.22 to 1.04 as the frequency increases. The steepest decrease of τ_{eff} occurs at $\hat{\omega}_L \sim 1.7$, the frequency at which the imaginary part of impedance is at its maximum. See the red dashed curve in Fig. 5(b). The frequency $\hat{\omega}_L \sim 1.7$ is between the two points near the top of the impedance curve in Fig. 5(a). There is a small hump near $\hat{\omega}_L \sim 12$, at which the impedance curve transitions to a straight line along 45°. See the point corresponding to $\hat{\omega}_L = 11.5$ in Fig. 5(a).

The behavior of τ_{eff} are explained as follows. At low frequencies, due to the long penetration depth, diffusers reach much of the entire microstructure. See the illustration in Fig. 6(a), which shows C_R at $\hat{\omega}_L = 0.39$ (the frequency near the end of the plateau of $\tau_{eff} \sim 1.22$, with the corresponding impedance marked by the red square in Fig. 5(a)). The gradients of concentration amplitude span over the entire microstructure, as evident in Fig. 6(a). The diffusion paths are tortuous, as illustrated by the white arrows in the same figure. Because of the additional path length that are required to diffuse through the microstructure, τ_{eff} is significantly larger than one.

As the frequency increases, the penetration depth is shortened. The diffusers are driven back and forth within a portion of the microstructure near the loading boundary. Figure 6(b) shows the concentration distributions at $\hat{\omega}_L = 89.07$, which corresponds to the impedance marked by the red triangle in Fig. 5(a). The active diffusion zone is confined below the green dashed line in Fig. 6(b). The concentration gradients above the green dashed line are very small. In this case, the diffusers only sample a fraction of the full microstructure, confined to the region near the loading boundary, as illustrated by the white arrow in Fig. 6(b). As a result, the effective tortuosity decreases. At extremely high frequencies, the penetration depth becomes smaller than the characteristic length scale of the channels in the microstructure. Diffusers

are then simply driven back and forth over a thin region near the loading boundary. Thus, τ_{eff} must approach one, as shown by the trend following the black curve in Fig. 5(c). Furthermore, as mentioned previously, the transition point between the semicircle and straight line on the impedance curve indicates a full decay of the concentration amplitudes within the domain such that the solution converges to that for the infinite-length domain. For this microstructure, this transition occurs at $\hat{\omega}_L \sim 11.5$, as indicated in Fig. 5(a). The slight increase of the effective tortuosity (the small hump on τ_{eff} in Fig. 5(c)) is a manifestation of the nonlinear nature of the cyclically driven diffusion in porous medium.

Using Eqs. (12) through (14), we derive the relationship between the impedance and effective tortuosity for the TBC case as

$$\frac{\left|Z^{3\mathrm{D}}\right|}{\left|Z^{\mathrm{FLW}}\right|} = \frac{1}{\varepsilon_v} \tau_{eff}^2,\tag{15}$$

where $Z^{\rm 3D}=Z_0/\tilde{D}_{eff}$ is the impedance for a porous solid that allows only bulk diffusion, and $Z^{\rm FLW}=Z_0/\tilde{D}^{\rm FLW}$ is the analytically calculated impedance from Eq. (14). As mentioned earlier, diffusion can only occur in a thin layer close to the loading boundary at extremely high frequencies. In such a case, the volume fraction of the region diffusion occurs must be close to the area fraction, ε_a , at the loading boundary. With $\tau_{eff} \approx 1$ at extremely high frequencies, Eq. (15) predicts $|Z^{3D}|/|Z^{FLW}| = 1/\varepsilon_a = 1.47$, where $\varepsilon_a = \int \psi dA|_{x=0}/A = 0.68$ for this microstructure. The blue circles in Fig. 5(c) exhibit such trend toward high frequencies. However, to quantitatively capture this behavior, simulations with much higher frequencies, which require very fine grid spacing, must be performed. We did not pursue such simulations because it would incur a large computational cost while gaining little additional insights. Furthermore, we have assumed that the volume fraction is uniform throughout the microstructure in the above analysis for simplicity, but in complex microstructures in physical samples, including the one considered here, there are variations in the volume fraction from one region to another. As a consequence, the diffusional impedance curve obtained from the full 3D calculation does not coincide with the one calculated by solving the 1D diffusion equation with a constant effective diffusivity obtained at zero frequency for the microstructure. This is evident in Fig. 5(d), in which the green circles are the impedance from the 3D calculation and the magenta dots are the impedance predicted from Eq. (8) with the effective

diffusivity determined at zero frequency. However, the difference is small for the microstructure considered in this work.

Furthermore, the frequency at which the imaginary part of the impedance is maximum, $\hat{\omega}_m$, shifts from 2.54 for the 1D case to 1.7 for the porous microstructure. This shift can be explained using the 1D analytical expression of diffusional impedance, Eq. (8). For a 1D diffusion case with a domain size L and diffusivity D, while the value of $\hat{\omega}_m$ cannot be analytically calculated [47], it can be numerically evaluated to be 2.54 [47]. When the domain size increases to 1.22L, the value of $\hat{\omega}_m$ changes to 1.73. This value is close to $\hat{\omega}_m$ of the porous microstructure with an average diffusion path length of 1.22L. Thus, we obtain the relationship:

$$\frac{\hat{\omega}_m^{\text{FLW}}}{\hat{\omega}_m^{\text{3D}}} = \frac{2.54}{1.7} \propto \left(\frac{L_D^{\text{3D}}}{L_D^{\text{FLW}}}\right)^2 = \tau_{eff}^2,\tag{16}$$

where L_D^{3D} and L_D^{FLW} can be viewed as the penetration depths at the corresponding $\hat{\omega}_m$ for the porous diffusion and bulk diffusion cases, respectively.

The SBM simulation results also exhibit the geometric effect on the local directions of diffusion. Figures 6(c) and (d) provide the magnified views of the gray dashed boxes in Fig. 6(a) and (b), respectively. Through bottleneck regions, the gradients of concentration amplitude turn along the neck directions, which can be clearly observed at the green arrows indicating the direction of the gradient, which parallels nearby surfaces. Moreover, the locations where the minima of C_R and C_I occur are approximately marked by the magenta lines in Figs. 6(b)-i and ii. The locations of maxima of C_I are closer to the loading boundary than that of C_R , similar to the case in the pseudo-1D calculations.

In summary, we find that, for a porous medium where only bulk diffusion occurs, the ratio between its diffusional impedance and that of a dense solid material reflects the effective tortuosity of the microstructure. This tortuosity is frequency-dependent because the loading frequency determines the depth of sampled microstructure.

3.4. Porous Cathode With Blocking Boundary

If the diffusers cannot cross the nonloading end of the sample, as in the case of a porous cathode with a blocking boundary, the reflective (no-flux) boundary condition is appropriate. Thus, we perform another set of simulations with the porous cathode microstructure using the reflective boundary

condition (RBC), where $\partial C_R/\partial x = \partial C_I/\partial x = 0$ is imposed at the nonloading side of the computational domain (x = 9.67). All other conditions are identical to the simulation presented in Section 3.3. Figure 7 shows two sets of representative concentration distributions, simulated for low-frequency and high-frequency responses. The real and imaginary concentration amplitudes at the low frequency ($\hat{\omega}_L = 0.72$), shown in Fig. 7(a)-i and -ii, respectively, are significantly different from those under the transmissive boundary condition (TBC). The no-flux boundary condition at x = 9.67 allows the values of C_R and C_I to be nonzero and to change in time at the nonloading boundary. Although C_R and C_I both monotonically decrease with increasing x, C_R at the boundary is much higher than that in Fig. 6(a), and C_I at x = 9.67 is substantially below zero. In contrast, the concentration-amplitude distributions at high frequency ($\hat{\omega}_L = 89.8$), shown in Fig. 7(b), are similar to those simulated under TBC, shown in Fig. 6(b), as expected because the boundary condition on the nonloading side does not alter the solution when the diffusion field does not reach it.

The impedance at various frequencies is calculated using the same method described in the previous sections. The resulting Nyquist plot with RBC is provided in Fig. 8(a), where the green circles are from the porous microstructure simulations, and the red circles are from pseudo-1D simulations. Figure 8(b) is the magnified view of the intermediate to high-frequency regions. The black curve is the analytical function for the FSW impedance plotted using Eq. (10). The red circles in Figs. 8(a) and (b) are the values of diffusional impedance, at various frequencies ranging from $0.13 < \hat{\omega}_L < 1.02 \times 10^3$, calculated using the pseudo-1D configuration as in Section 3.2, but with the reflective boundary condition. Again, the pseudo-1D results agree well with the analytical solution.

The calculated impedance curve (green circles) for the porous cathode microstructure at the same frequencies as in the pseudo-1D case exhibits a similar shape to that of the analytical solution for FSW as well as the pseudo-1D results, showing a vertical straight line at low frequencies and a 45°-line at high frequencies. The impedance curve in the high-frequency region is similar to that for the case with TBC (Fig. 5(a)). This behavior can also be supported by the similarity of the concentration distributions between the case with TBC (Fig. 6(b)) and the case with RBC (Fig. 7(b)). However, the calculated impedance (green circles) of the porous microstructure is generally larger than that of the 1D FSW values, as shown in Fig. 8(b), in which the green circles are on the right of the solid curve for low frequencies are above

the the solid curve for high frequencies. This behavior is consistent with physical intuition because the porous medium has less volume for diffusion compared to the dense solid, leading to a larger impedance unless other transport mechanisms, such as surface diffusion, take place. Consideration of additional mechanisms are beyond the scope of this paper, and will be a topic of future work.

As in the analysis presented in Section 3.3, the ratio between the diffusional impedance of the porous microstructure and the analytical 1D case are calculated and plotted with the blue squares on Fig. 8(c). The curve shows that $|Z^{3D}|/|Z^{FSW}|$ asymptotically approaches a certain value as the frequency decreases in the low-frequency region. The value for the lowest frequency ($\hat{\omega}_L = 0.13$) in the calculation is approximately 1.581, which is close to the inverse of the volume fraction of the solid phase in the microstructure, 1.577. This value can be explained based on Eq. (10). Assuming $L\sqrt{i\omega/D} \ll 1$ at low frequencies, the FSW impedance can be approximated using the Taylor expansion of hyperbolic cotangent around zero as [43, 48]

$$Z^{\text{FSW}} \approx \frac{RTL}{z^2 F^2 D c_0 A} \cdot \left(\frac{D}{L^2} \frac{1}{i\omega} + \frac{1}{3}\right).$$
 (17)

For low frequencies, the first term in the parenthesis dominates the value of impedance. Thus, the impedance will be inversely proportional to AL, the volume of the domain. As a result, at the same loading frequency, the diffusional impedance with RBC is inversely proportional to the volume fraction of the diffusion zone, such that

$$\frac{\left|Z^{\text{3D}}\right|}{\left|Z^{\text{FSW}}\right|} \approx \frac{1}{\varepsilon_{v}}.$$
 (18)

In the region of intermediate frequency, the curve of $|Z^{3D}|/|Z^{FSW}|$ exhibits a peak, which corresponds to the region where the impedance curves of the porous microstructure and the 1D case transition to the 45°-lines (see the markers corresponding to $\hat{\omega}_L = 4.84$ in Figs. 8(b) and (c)).

For high frequencies, assuming $L\sqrt{i\omega/D}\gg 1$, Eq. (10) can be approximated as

$$Z^{\text{FSW}} \approx \frac{RTL}{z^2 F^2 D c_0 A} \cdot \frac{1}{L} \sqrt{\frac{D}{i\omega}}.$$
 (19)

Thus, at the same loading frequency, the impedance is inversely proportional to the area where diffusers are inserted to or extracted from the solid. For

the porous microstructure examined in the work, we expect

$$\frac{\left|Z^{3\mathrm{D}}\right|}{\left|Z^{\mathrm{FSW}}\right|} \approx \frac{1}{\varepsilon_a} = 1.47\tag{20}$$

at very high frequencies. Note that the analysis of Eq. (19) and the prediction of Eq. (20) also apply to the TBC case because both FLW and FSW converge to IW at very high frequencies. As can be inferred from the trend shown in Fig. 8(c), $|Z^{3D}|/|Z^{FSW}|$ decreases and approach the expected value as the frequency increases in the high-frequency region. For the highest frequency $(\hat{\omega}_L = 1.02 \times 10^3)$ in the calculation, we obtain $|Z^{3D}|/|Z^{FSW}| = 1.52$, which is still larger than 1.47. This deviation implies that a higher loading frequency is required for further convergence to the expected value. However, simulations for extremely high frequencies will require higher resolution for the spatial discretization than that employed in this work for sufficient numerical accuracy. Since little additional insight can be gained and our results are already within 3.5% of the expected value, we do not pursue simulations with extremely high loading frequencies.

3.5. Impedance of Battery Cathode

In Sections 3.3 and 3.4, the primary diffusion direction is from the loading to the nonloading boundaries (i.e., in the positive x-direction). However, in battery electrodes, the diffusion direction becomes from the surfaces to the centers of individual electrode particles, leading to a significantly different process. Thus, we apply Eq. (7) to calculate the diffusional impedance of an experimentally reconstructed laptop battery cathode microstructure to demonstrate the versatility of SBM. The details of microstructure reconstruction can be found in Ref. [49]. In this calculation, the concentration is specified to be $C_R^B=1$ and $C_I^B=0$ on the particle surfaces without loss of generality. The grid spacing and computational domain boundary conditions are kept the same as in Section 3.4. Figures 9(a) and (b) show the calculated Nyquist plot, where (b) is the magnified view in the high frequency region of (a). The impedance computed at various frequencies is marked with the green circles. The shape of the calculated impedance curve (green circles) corresponds to that of a capacitive diffusional impedance and is over all similar to that in Section 3.4 (see the impedance curve in Figs. 8(a) and (b), calculated with RBC using the SOFC microstructure). The black circles on the same plot are the analytical FSW impedance at the same frequencies corresponding to the green ones. The FSW values are calculated based

on a sphere having a radius of 34 μ m (the average particle radius of this cathode microstructure). The impedance of the battery cathode is shifted significantly to the right of the analytical curve. This deviation indicates that the interconnected microstructure cannot be simply represented by a sphere of the average radius when interpreting EIS data even when only the diffusional contribution is considered. The complex concentration amplitude distributions at $\hat{\omega}_L = 23.84$, corresponding to the blue triangle on Fig. 9(b), are shown in Fig. 9(c) and (d). Their variation can be considered similar to what will happen in the FSW case (e.g., Fig. 7(b)). Along the primary diffusion direction, the amplitudes decrease rapidly near the loading surface but smoothly increases back further away from the loading surface. The major difference is now the primary diffusion direction is towards the particle centers. Nevertheless, the non-uniform sizes, irregular shapes, and connections between particles complicate the concentration distribution. As a result, each individual particle behaves differently. We here aim only to demonstrate the importance of explicit consideration of the microstructural effect; detailed analysis will be considered in the future. While the discrepancy between the impedance of the porous cathode and that analytical calculated for a sphere at low to intermediate frequencies is attributed to the microstructural effect, the deviation at high frequencies may also include some numerical errors due to the lack of grid resolution mentioned in the previous sections.

Finally, we note that while we focus only on bulk diffusion in this work, the SBM allows incorporation of other mechanisms, such as surface diffusion and surface reaction [34] on irregular particle surfaces. Further investigation of those coupled mechanisms in the EIS is left for future work.

4. Conclusion

In this paper, we employed the smoothed boundary method to simulate diffusion through an experimentally obtained 3D microstructure from a porous SOFC cathode sample. The real and imaginary components of the concentration response to sinusoidal loadings are obtained for various frequencies, which are used to calculate the diffusional impedance. When a nonblocking (transmissive) boundary condition is imposed on the boundary opposite to the loading boundary, the impedance value is a function of the tortuosity within the diffusion zone of the sample. At low frequencies, this diffusion zone spans nearly the entire domain. Thus, the measured diffusional impedance, along with the analytically calculated finite-length War-

burg impedance, yields the tortuosity factor of the entire porous medium. At high frequencies, tortuosity of the diffusion zone approaches unity because diffusion only occurs within a thin layer close to the loading boundary and this distance becomes smaller than the characteristic length scale of the porous medium. On the other hand, when a blocking (reflective) boundary condition is imposed on the boundary opposite to the loading boundary, the diffusional impedance at low frequencies is inversely proportional to the volume fraction of the solid phase. At high frequencies, the impedance is inversely proportional to the ratio between contact area and the nominal area of the loading boundary. The simulation results presented here demonstrate that the diffusional impedance spectroscopy can be utilized to probe microstructural characteristics such as the porosity and contact area of the loading boundary.

Acknowledgement: Authors thank J. Scott Cronin for his assistance with the use of the 3D microstructural data. This work is support by the United States National Science Foundation, Division of Material Research, Ceramics Program, under the grant numbers DMR-1506925 (SB) and DMR-1506055 (KT). Computational resources were provided by the Extreme Science and Engineering Discovery Environment (XSEDE [50]) (allocation No. TG-DMR110007), which is supported by the United States National Science Foundation under grant number ACI-1053575, by the National Energy Research Scientific Computing Center (NERSC), a DOE Office of Science User Facility supported by the Office of Science of the U.S. Department of Energy under Contract No. DE-AC02-05CH11231, and also by the University of Michigan Advanced Research Computing.

References

- [1] M. E. Orazem, B. Tribollet, Electrochemical Impedance Spectroscopy, John Wiley & Sons, 2008.
- [2] A. A. Moya, A numerical exercise to teach electrochemical impedance using electric circuit simulation software, Journal of Chemical Education 90 (2013) 1699–1700.
- [3] F. Ciucci, Electrochemical impedance spectroscopy of porous electrodes: the effect of pore size distribution, Current Opinion in Electrochemistry 13 (2019) 132–139.

- [4] D. R. Franceschetti, J. R. Macdonald, R. P. Buck, Interpretation of finite-length-warburg-type impedances in supported and unsupported electrochemical cells with kinetically reversible electrodes, Journal of Electrochemical Society 138 (1991) 1368–1371.
- [5] J. R. Macdonald, D. R. Franceschetti, Precision of impedance spectroscopy estimates of bulk, reaction rate, and diffusion parameters, Journal of Electroanalytical Chemistry 307 (1991) 1–11.
- [6] G. Barbero, I. Lelidis, Analysis of warburg's impedance and its equivalent electric circuits, Physical Chemistry Chemical Physics 19 (2017) 24934–24944.
- [7] G. Barbero, Theoretical interpretation of warburg's impedance in unsupported electrolytic cells, Physical Chemistry Chemical Physics 19 (2017) 2575–32579.
- [8] J. Huang, Diffusion impedance of electroactive materials, electrolytic solutions and porous electrodes: Warburg impedance and beyond, Electrochimica Acta 281 (2018) 170–188.
- [9] E. Warburg, Ueber das verhalten sogenannter unpolarisirbarer elektroden gegen wechselstrom, Annalen der Physik und Chemie 67 (1899) 493–499.
- [10] A. Honders, G. H. J. Broers, Bounded diffusion in solid solution electrode powder compacts part i the interfacial impedance of a solid solution electrode (mxsse) in contact with a m+-ion conducting electrolyte, Solid State Ionics 15 (1985) 173–183.
- [11] I. D. Raistrick, D. R. Franceschetti, J. R. Macdonald, Impedance Spectroscopy, John Wiley & Sons Inc., Hoboken, New Jersey, pp. 56–57.
- [12] C. Ho, I. D. Raistrick, R. A. Huggins, Application of a-c techniques to the study of lithium diffusion in tungsten trioxide thin films, Journal of the Electrochemical Society 127 (1980) 343–350.
- [13] B. A. Boukamp, Electrochemical impedance spectroscopy in solid state ionics: recent advances, Solid State Ionics 169 (2004) 65–73.

- [14] M. D. Levi, D. Aurbach, Frumkin intercalation isotherm a tool for the description of lithium insertion into host materials: a review, Electrochimica Acta 45 (1999) 167–185.
- [15] M. D. Levi, D. Aurbach, Impedance of a single intercalation particle and of non-homogeneous, multilayered porous composite electrodes for li-ion batteries, Journal of Physical Chemistry B 108 (2004) 11693–11703.
- [16] H. Keiser, K. D. Beccu, M. A. Gutjahhr, Abschätzung der porenstruktur poröser elektroden aus impedanzmessungen, Electrochimica Acta 21 (1976) 539–543.
- [17] I. D. Raistrick, Impedance studies of porous electrodes, Electrochimica Acta 35 (1990) 1579–1586.
- [18] H.-K. Song, Y.-H. Jung, K.-H. Lee, L. H. Dao, Electrochemical impedance spectroscopy of porous electrodes: the effect of pore size distribution, Electrochimica Acta 44 (1999) 3513–3519.
- [19] R. Jurczakowski, C. Hitz, A. Lasia, Impedance of porous au based electrodes, Journal of Electroanalytical Chemistry 572 (2004) 355–366.
- [20] H.-K. Song, J.-H. Sung, Y.-H. Jung, K.-H. Lee, L. H. Dao, M.-H. Kim, H.-N. Kim, Electrochemical porosimetry, Journal of the Electrochemical Society 151 (2004) E102–E109.
- [21] D. D. Macdonald, Reflections on the history of electrochemical impedance spectroscopy, Electrochimica Acta 51 (2006) 1376–1388,.
- [22] U. Tröltzsch, O. Kanoun, Generalization of transmission line models for deriving the impedance of diffusion and porous media, Electrochimica Acta 75 (2012) 347–356,.
- [23] J. Landesfeind, J. Hattendorff, A. Ehrl, W. A. Wall, H. A. Gasteiger, Tortuosity determination of battery electrodes and separators by impedance spectroscopy, Journal of the Electrochemical Society 163 (2016) A1373—A1387.
- [24] F. Hilario, V. Roche, A. M. Jorge Junior, R. P. Nogueira, Application of the transmission line model for porous electrodes to analyse the impedance response of tio2 nanotubes in physiological environment, Electrochimica Acta 253 (2017) 599–608.

- [25] M. Doyle, J. P. Meyers, J. Newman, Computer simulations of the impedance response of lithium rechargeable batteries, Journal of the Electrochemical Society 147 (2000) 99–110.
- [26] S. Devan, V. R. Subramanian, R. E. White, Analytical solution for the impedance of a porous electrode, Journal of the Electrochemical Society 151 (2004) A905–A913.
- [27] J. G. Zhu, Z. C. Sun, X. Z. Wei, H. F. Dai, A new electrochemical impedance spectroscopy model of a high-power lithium-ion battery, RSC Advances 4 (2014) 29988–29998.
- [28] J. Song, M. Z. Bazant, Effects of nanoparticle geometry and size distribution on diffusion impedance of battery electrodes, Journal of the Electrochemical Society 160 (2012) A15–A24.
- [29] J. Song, M. Z. Bazant, Electrochemical impedance of a battery electrode with anisotropic active particles, Electrochimica Acta 131 (2014) 214– 227.
- [30] C. R. Kreller, M. E. Drake, S. B. Adler, Influence of electrode morphology on electrochemical response of sofc cathodes, ECS Transactions 28 (2010) 105–121.
- [31] S. Cho, C. F. Chen, P. P. Mukherjee, Influence of microstructure on impedance response in intercalation electrodes, Journal of the Electrochemical Society 162 (2015) A1202–A1214.
- [32] S. J. Cooper, A. Bertei, D. P. Finegan, N. P. Brandon, Simulated impedance of diffusion in porous media, Electrochimica Acta 251 (2017) 681–689.
- [33] S. J. Cooper, A. Bertei, P. R. Shearing, J. A. Kilner, N. P. Brandon, Taufactor: An open-source application for calculating tortuosity factors from tomographic data, SoftwareX 5 (2016) 203–210.
- [34] H.-C. Yu, H.-Y. Chen, K. Thornton, Extended smoothed boundary method for solving partial differential equations with general boundary conditions on complex boundaries, Modelling and Simulation in Materials Science and Engineering 20 (2012) 075008.

- [35] R. Amin, Y.-M. Chiang, Characterization of electronic and ionic transport in $li_{1-x}ni_{0.33}mn_{0.33}co_{0.33}o_2$ (nmc333) and $li_{1-x}ni_{0.50}mn_{0.20}co_{0.30}o_2$ (nmc523) as a function of li content, Journal of the Electrochemcial Society 163 (2016) A1512–A1517.
- [36] J. P. Schmidt, P. Berg, M. Schönleber, A. Weber, E. Ivers-Tiffée, The distribution of relaxation times as basis for generalized time-domain models for li-ion batteries, Journal of Power Sources 221 (2013) 70–77.
- [37] T. R. Ferguson, M. Z. Bazant, Nonequilibrium thermodynamics of porous electrodes, Journal of Electrochemical Society 159 (2012) A1967– A1985.
- [38] Y. Lu, C. Kreller, S. Adler, Measurement and modeling of the impedance characteristics of porous la1xsrxcoo3d electrodes, Journal of the Electrochemical Society 156 (2009) B513–B525.
- [39] E. F. Van de Velde, Concurrent Scientific Computing, Springer-Verlag, New York, 1st edition, p. 202.
- [40] J. Hofhaus, E. F. Van de Velde, Alternating-direction line-relaxation methods on multicomputers, SIAM Journal on Scientific Computing 17 (1996) 454–478.
- [41] J. R. Wilson, W. Kobsiriphat, R. Mendoza, H.-Y. C. Chen, T. Hines, J. M. Hiller, D. J. Miller, K. Thornton, P. W. Voorhees, S. B. Adler, D. Mumm, S. A. Barnett, Three dimensional reconstruction of solid oxide fuel cell electrodes using focused ion beam - scanning electron microscopy, ECS Transactions 7 (2007) 1879–1887.
- [42] C. L. Park, P. W. Voorhees, K. Thornton, Application of the level-set method to the analysis of an evolving microstructure, Computational Materials Scienceputational 85 (2014) 46–58.
- [43] J. Bisquert, G. Garcia-Belmonte, F. Fabregat-Santiago, P. R. Bueno, Theoretical models for ac impedance of finite diffusion layers exhibiting low frequency dispersion, Journal of Electroanalytical Chemistry 475 (1999) 152–163.

- [44] J. P. Diard, B. Le Gorrec, C. Montella, Theoretical models for ac impedance of finite diffusion layers exhibiting low frequency dispersion, Journal of Electroanalytical Chemistry 471 (1999) 126–131.
- [45] J. Crank, The Mathematics of Diffusion, Oxford University Press, 2nd edition, 1975.
- [46] N. Epstein, On tortuosity and the tortuosity factor in flow and diffusion through porous media, Chemical Engineering Science 44 (1989) 777–779.
- [47] J. L. Dawson, D. G. John, Diffusion impedance an extended general analysis, Journal of Electroanalytical Chemistry and Interfacial Electrochemistry 110 (1980) 37–47.
- [48] J. Torben, K. West, Diffusion impedance in planar, cylindrical and spherical symmetry, Electrochimica Acta 40 (1995) 255–262.
- [49] J. R. Wilson, J. S. Cronin, S. A. Barnett, S. J. Harris, Measurement of three-dimensional microstructure in a licoo2 positive electrode, Journal of Power Sources 196 (2011) 3443–3447.
- [50] J. Towns, T. Cockerill, M. Dahan, I. Foster, K. Gaither, A. Grimshaw, V. Hazlewood, S. Lathrop, D. Lifka, G. D. Peterson, R. Roskies, J. R. Scott, N. Wilkens-Diehr, Xsede: Accelerating scientific discovery, Computing in Science and Engineering 16 (2014) 62–74.

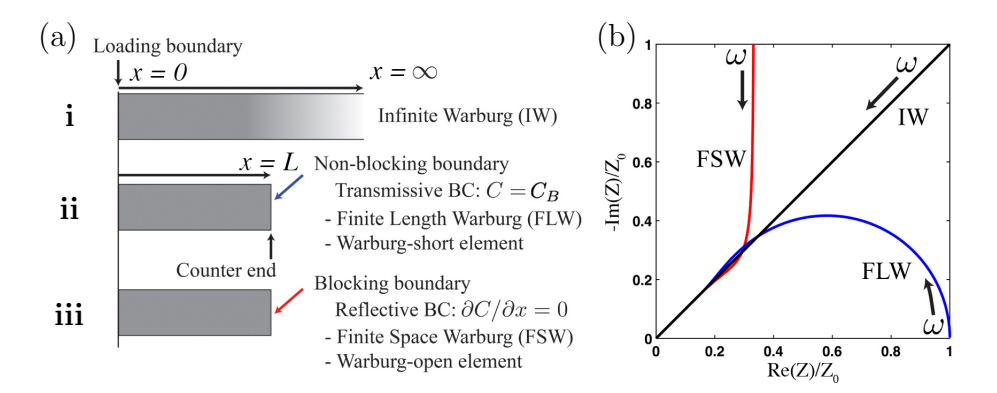


Figure 1: Illustration of the three types of Warburg impedance. (a) The domains for diffusion and boundary conditions for: (i) the infinite Warburg, (ii) finite-length Warburg, and (iii) finite-space Warburg impedance. (b) Nyquist plot for the IW, FLW, and FSW impedance. The black arrows indicate the directions along which the impedance varies as the loading frequency increases.

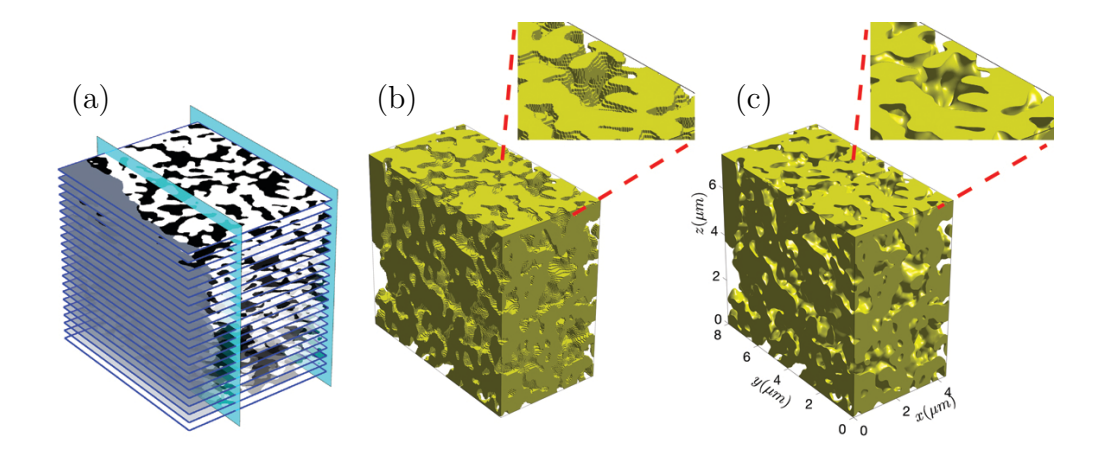


Figure 2: Acquisition of the input geometry for SBM simulation. (a) Schematic illustration of image stacking for microstructure reconstruction. The white, gray, and black pixels indicate LSC, GDC, and pore phases, respectively. The cathode microstructure between the two cyan planes are used for the simulations. (b) The voxelated microstructure between the two cyan planes in (a). The magnified view shows the zigzag, stepped cathode microstructure surfaces. (c) The isosurfaces of $\psi=0.5$. The surfaces are smoother than that in (b). The x=0 boundary corresponds to the loading boundary. The opposite boundary can be either blocking or nonblocking.

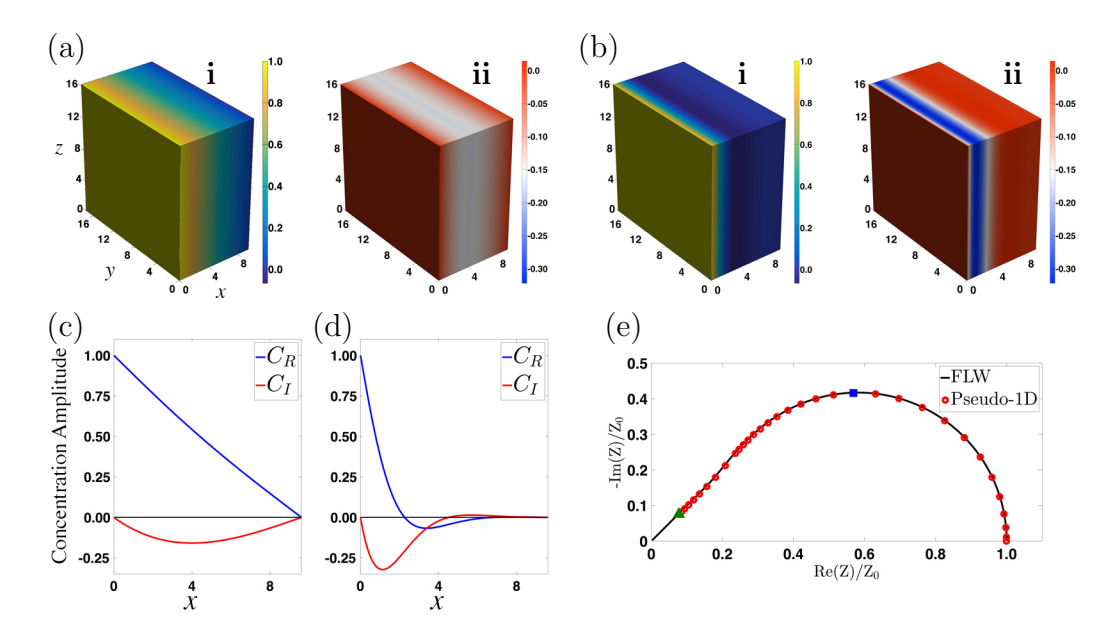


Figure 3: The concentration distributions under AC loads at frequencies equal to (a) $\hat{\omega}_L = 2.65$, (b) $\hat{\omega}_L = 89.07$, where subfigures (i) and (ii) are for C_R and C_I , respectively. (c) and (d) are the profiles along the diffusion direction corresponding to (a) and (b), respectively. (e) The Nyquist plot of simulated dimensionless impedance for the pseudo-1D calculations with TBC and analytical solution of FLW. The blue square and green triangle correspond to (a) and (b), respectively.

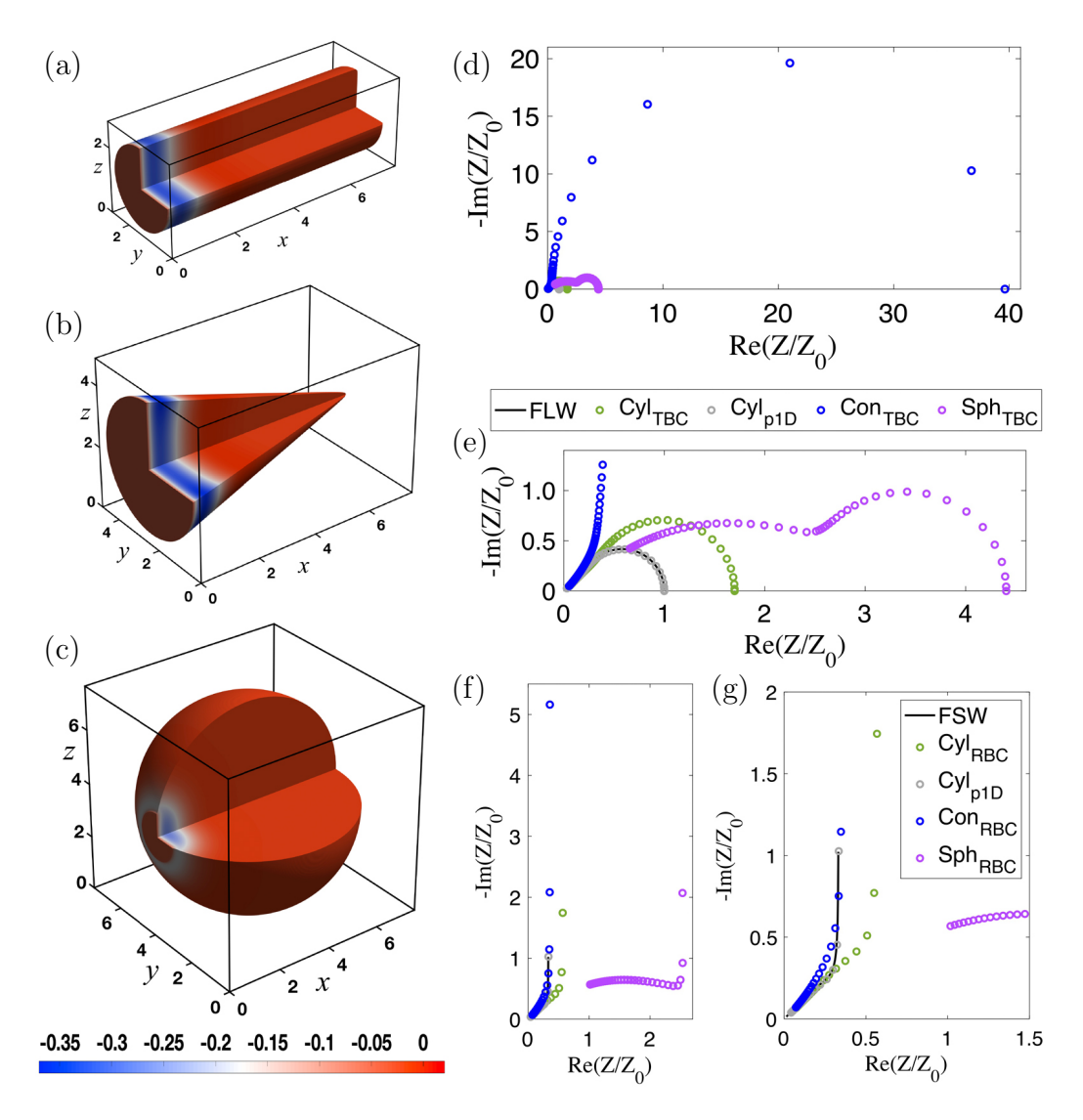


Figure 4: Subfigures (a), (b), and (c) show the geometries of the cylinder, cone, and sphere, respectively, used in the simulations. A quarter of the volume in each geometry is made transparent to show the concentration distribution inside the object. The colors indicate the C_I distribution at $\hat{\omega}_L = 256$ calculated with RBC. (d) Nyquist plot of the diffusional impedance with TBC for the geometries, and (e) magnified view of (d) near the origin. (f) Nyquist plot of the diffusional impedance with RBC, and (g) magnified view of (f) near the origin. The green, blue, and purple circles are for the cylinder, cone, and sphere, respectively. The gray circles are impedance of the cylinder normalized to the cylinder cross-section area, which overlap with the analytical values of FLW and FSW impedance shown by the black curves.

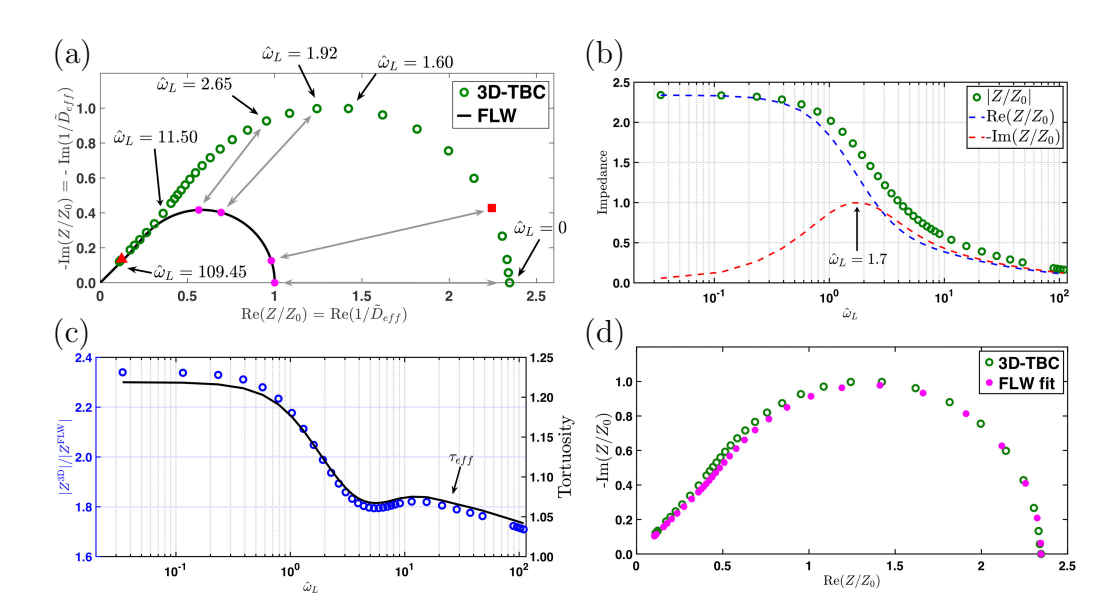


Figure 5: (a) Dimensionless impedance curve for the porous microstructure. The black curve is for FLW. The four magenta points are for $\hat{\omega}_L=0$, 0.39, 1.92, and 2.65 from the right to left. The gray arrows point to the data points for porous solid at the same frequencies. (b) The Bode plot of the amplitude, real and imaginary parts of the calculated impedance. The impedance is the reciprocal of \tilde{D}_{eff} , the complex effective diffusivity of the microstructure. (c) The effective tortuoisty (black line) and ratio of $|Z^{3D}|/|Z^{FLW}|$ (blue circles) as functions of frequency. (d) The comparison between the diffusional impedance obtained from the full 3D calculation (green circles) and the FLW impedance (magenta dots) calculated with the effective diffusivity obtained at zero frequency. The circles and dots correspond to the same frequencies.

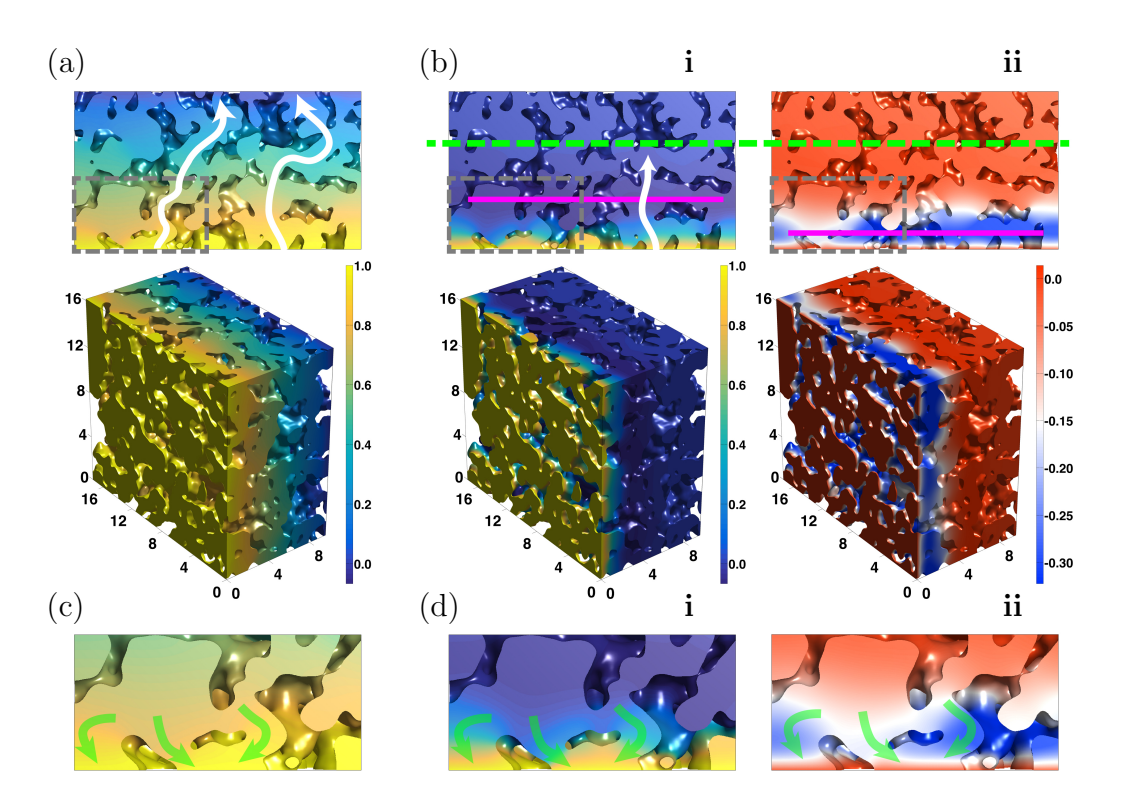


Figure 6: Complex concentration amplitudes evaluated with the transmissive boundary condition on the nonloading end for frequencies (a) $\hat{\omega}_L = 0.39$ and (b) $\hat{\omega}_L = 89.07$. Only C_R is shown in (a) because the variation of C_I at $\hat{\omega}_L = 0.39$ is small. The subfigures (i) and (ii) are for C_R and C_I , respectively. The top row shows the top view of the computational domain. The impedance corresponds to (a) and (b) are marked by the red square and triangle in Fig. 5(a), respectively. The green dash line indicates the approximate extent of diffusion, and the magenta line indicates the approximate position where the respective component of the concentration amplitude is minimum. (c) and (d) the magnified views of the gray boxes in (a) and (b), respectively. The green arrows highlight how the direction of the concentration gradient changes with the orientation of the diffusion channels.

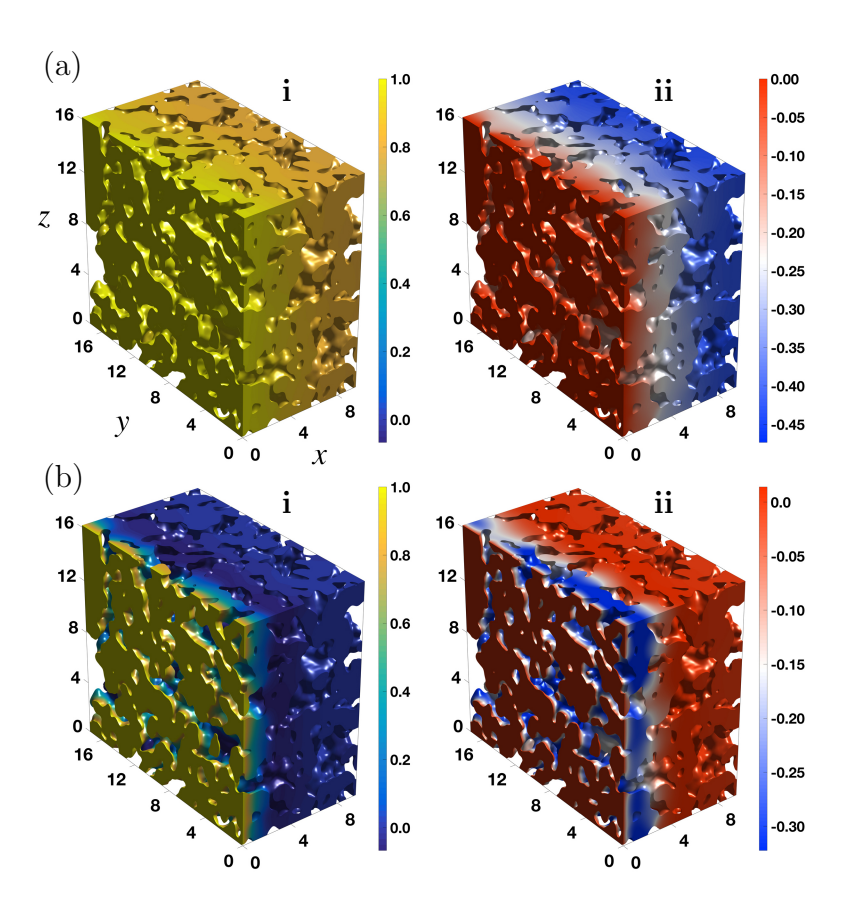


Figure 7: Complex concentration amplitudes evaluated with the reflective boundary condition on the nonloading end for frequencies (a) $\hat{\omega}_L=0.72$ and (b) $\hat{\omega}_L=89.8$. The subfigures i and ii are the real and imaginary components, respectively.

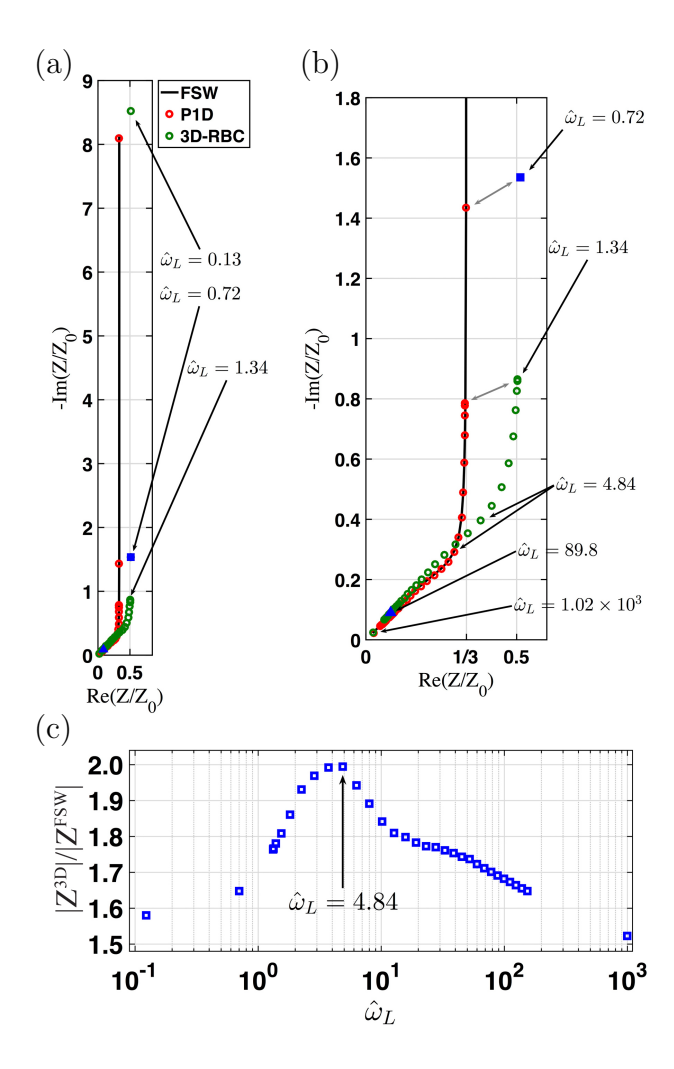


Figure 8: (a) The Nyquist plot for the simulated diffusion impedance at various frequencies with reflective boundary condition. The green and red circles are from the porous microstructure and pseudo-1D simulations with the reflective boundary condition, respectively. The black curve is the analytic value for FSW impedance. (b) Magnified view for the intermediate to high frequency regions of (a). The blue square and triangle are the impedance corresponding to Fig. 7(a) and (b), respectively. (c) The values of $\left|Z^{\rm 3D}\right|/\left|Z^{\rm FSW}\right|$ at different frequencies, where $Z^{\rm 3D}$ and $Z^{\rm FSW}$ are the calculated impedance for the porous microstructure and the analytically calculated FSW impedance, respectively.

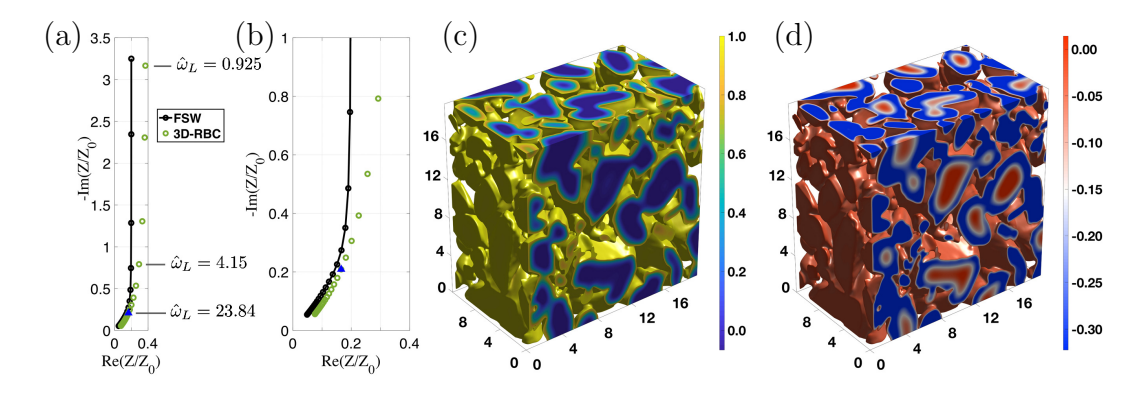


Figure 9: (a) Nyquist plot for the simulated diffusion impedance of a battery cathode, and (b) the high frequency region of (a). The concentration amplitudes of (c) C_R and (d) C_I in the cathode microstructure at frequency $\hat{\omega}_L = 23.84$, corresponding to the blue triangle in (a) and (b).